ISSN 1392-1207. MECHANIKA. Vol. 31, No. 2, 2025: 136–149

Optimization of Static Three-Dimensional Stiffness of Non-Pneumatic Tire with Composite Spokes Based on Response Surface Method

Jingcun LIANG*, Xiaotong LIU, Xianjia WU***, Muyang SUN****, Yuxin SONG*****, Weidong LIU******, Qiushi ZHANG*********
**College of Automotive Engineering, Jilin University, Changchun, 130022, China, E-mail: liangjc1522@mails.jlu.edu.cn*
***College of Automotive Engineering, Jilin University, Changchun, 130022, China, E-mail: liuxt1521@mails.jlu.edu.cn*
****College of Automotive Engineering, Jilin University, Changchun, 130022, China, E-mail: wuxj1722*@mails.jlu.edu.cn
*****College of Automotive Engineering, Jilin University, Changchun, 130022, China,*
E-mail: sunmy1521@mails.jlu.edu.cn
******College of Automotive Engineering, Jilin University, Changchun, 130022, China,*
E-mail: songyx1523@mails.jlu.edu.cn
*******College of Automotive Engineering, Jilin University, Changchun, 130022, China,*
E-mail: wdliu@jlu.edu.cn
********College of Automotive Engineering, Jilin University, Changchun, 130022, China,*
E-mail: qszhang@jlu.edu.cn (Corresponding Author)

https://doi.org/10.5755/j02.mech.40367

1. Introduction

With increasing demands for safety, stability, and comfort in automobiles, more stringent requirements for tire safety and durability are being emphasized. In response to these demands, non-pneumatic tires (NPTs) are gaining favor owing to advantages such as puncture resistance and blowout prevention. In 2006, Michelin pioneered the concept of the NPT [1] and introduced the Tweel NPT [2]. Resilient Technologies, in collaboration with the University of Wisconsin, developed a biomimetic honeycomb NPT by applying a hexagonal honeycomb structure to tire spokes [3]. In 2012, a re-search team led by Zhao Youqun at the Nanjing University of Aeronautics and Astronautics designed a mechanical elastic wheel (MEW) with a hinged structure [4]. In 2010, Kim et al. designed negative Poisson's ratio notched hexagonal airless tire [5]. In 2019, Michelin and General Motors jointly introduced the UPTIS NPT, achieving a groundbreaking innovation in tire structures and composite materials. It is anticipated that UPTIS will be widely applied in passenger vehicles by 2024 [6].

In recent years, research on the load-bearing performance of NPTs has primarily focused on shear bands and spokes. In 2010, Gasmi et al. utilized curved beam theory to analyze ring-ground contact and derive control equations based on virtual work principles. Three stiffness parameters (EI, GA, and EA) were investigated to determine their influence on the contact pressure [7]. In 2012, they proposed an analytical model for compliant NPTs on frictionless rigid ground using a thin flexible ring connected to a rigid hub via spokes. The model, based on curved beam theory, analyzed deformations and could conduct a comprehensive parameter analysis for NPTs [8]. In 2018, Rugsaj et al. developed a hyperelastic material model for the finite element (FE) analysis of NPTs using Michelin's Tweel. The model was based on tensile and compressive test samples, and the stress–strain relationship was fitted to select an appropriate constitutive model [9]. In 2019, they developed FE models (FEMs) with different spoke shapes for NPTs to assess the geometric influences on stiffness and local stresses. The analysis identified the optimal spoke structure for the load-bearing capacity of NPTs [10]. Extensive research has indicated that the mechanical performance of NPTs varies significantly with different spoke forms. Researchers have utilized experimental methods and FE simulations to study the load-bearing capacity and stiffness of NPTs with various spoke structures. In 2019, Rugsaj et al. developed a three-dimensional FEM for Tweel NPTs, optimizing radial spokes for a vertical stiffness approximation through comparison with physical experiments [11]. In the same year, Żmuda et al. conducted a numerical study on the Tweel NPT model, simulating various values of normal force loads and documenting the shape of the contact area of the NPT on rigid ground [12]. In 2020, Żmuda et al. studied the mechanical performance of Tweel NPTs and analyzed the impact of the thickness and material using seven geometric shapes in simulated tests to determine the radial stiffness and unit pressure in the contact area [13]. In 2018, Jin et al. examined NPTs with different honeycomb spokes and discovered lower stress in spokes and treads compared with traditional tires, and a higher load-carrying capacity for NPTs [14]. In 2019, Ganniari-Papageorgiou et al. designed a parameterized FEM for honeycomb NPTs and found that the vertical stiffness was strongly influenced by the honeycomb unit density, thickness, and internal angle [15]. In 2018, Zhao et al. designed four MEWs with varying hinge structures and studied their static stiffness characteristics through numerical simulations and experiments. The nonlinear FEM was validated via tests on the load characteristics, and vertical, longitudinal, lateral, and torsional stiffness tests were conducted on the MEWs and in-flatable tires, with a thorough comparison and analysis of the experimental and simulation data [16]. In 2013, Lee et al. studied the dynamic characteristics of flexible expanding hexagonal mesh spokes for NPTs using an FEM to analyze the relationship between the angular velocity, displacement at the hub center, and ground reaction force during steady rolling [17]. In 2023, Liu et al. designed high-load-capacity NPTs (HC tires) and assessed their static stiffness through experiments and numerical simulations using a comprehensive tire stiffness tester. They validated the accuracy of a nonlinear FEM using vertical stiffness tests [18]. As evidenced, NPTs currently exhibit various developmental forms, and FE analysis methods are crucial research tools for studying these NPTs.

Currently, Michelin's new-generation NPTs, the UPTIS, have significant innovation and development potential. In 2022, Liang et al. modeled an UPTIS prototype tire and studied its load characteristics and mechanical performance under radial and combined forces through a three-dimensional numerical analysis [19]. In 2021, Dhrangdhariya et al. compared the Tweel, honeycomb, and newly developed UPTIS and examined the influence of material nonlinearity on different spoke designs [20]. In 2023, they developed an FEM to assess UPTIS NPT spokes and optimized their design to enhance the stiffness and damage resistance performance [21]. Existing patent in-formation highlights the distinct feature of UPTIS: spokes composed of composite materials. Conventional studies often overlook the impact of applying composites on the mechanical performance of NPTs, assuming homogeneous spoke materials [6].

A wealth of research indicates that the stiffness characteristics and load-bearing capacity of NPTs are closely related to their material composition and geometric parameters. Therefore, when studying the design parameters and mechanical properties of NPTs, selecting appropriate data analysis methods is crucial for optimizing NPT designs. In 2015, Kim et al. optimized the geometric shape of honeycomb NPTs using an FEM and design of experiments. They determined the impact of design variables on the rolling resistance, employed vertical deflection and contact pressure as constraints, and determined an optimal design through a response surface model [22]. In 2022, Liu et al. focused on spoke design for Fibonacci spiral NPTs (FS-NPT) and analyzed three-dimensional stiffness through FE modeling and design of experiments. Using a response surface model, they aimed to achieve lightweighting by minimizing mass while maintaining vertical stiffness [23]. It is evident that response surface analysis and multi-objective optimization are crucial methods for guiding the design of NPTs.

Although extensive research has been conducted on the load-bearing capacity and stiffness characteristics of NPTs with different structural forms and material properties, most of these studies have focused on NPTs composed of a single homogeneous material, without considering the application of composite materials in NPTs. There-fore, this study considered the UPTIS structure as an example. Tensile experiments were conducted on its elastomeric material (Section 2), utilizing the neo-Hookean model to construct a hyperelastic constitutive model of the elastomeric material based on experimental data, and an FEM was established for the UPTIS structure composed of composite materials. The boundary conditions for the loading were set according to the operating conditions of the NPT (Section 3). By conducting multiple simulation experiments on the NPT with different design parameters, fitting a mathematical model of the three-axis stiffness of the NPT based on the experimental results, per-forming a sensitivity analysis, inferring the load-carrying mechanism of the NPT, and determining the design parameters that have a significant impact on the three-axis stiffness of the NPT, the three-axis stiffness of the NPT could be predicted using mathematical methods. Subsequently, based on the desired stiffness requirements, the design parameters of the NPT were optimized through mathematical prediction to obtain an NPT design that satisfied the usage requirements.

2. Material Property Testing

In the existing literature and patents, Michelin UPTIS tires have been documented to employ distinct rubber formulations tailored to various structural components based on the performance requirements. Additionally, the corresponding skeletal structures were incorporated into the spokes and shear bands. To precisely depict the mechanical characteristics of rubber materials, this study opted for commonly used rubber materials in spokes and performed uniaxial tensile tests to reverse evaluate the hyperelastic constitutive model parameters. The rubber specimens were derived from vulcanized plate sheets with a thickness of 2 mm, as shown in Fig. 1. The specimens had a gauge length of 25 mm and width of 6 mm.

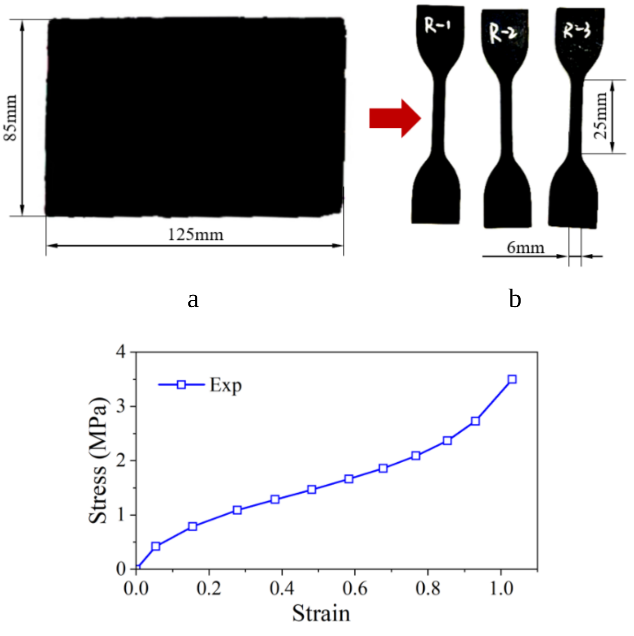

c

Fig. 1 Rubber tensile test: a – flat specimen, b – dumbbell-shaped tensile specimen, c – engineering stress-strain curve

The stress–strain curve acquired from the tensile test confirmed the hyperelastic mechanical behavior of the rubber, as illustrated in Fig. 1. The material demon-strated elastic behavior across various segments of the curve, preserving elasticity even at higher strain values and autonomously recovering to its initial state after un-loading. The hyperelastic constitutive model applied to the rubber material of the UPTIS NPT in this study used the stress–strain curve obtained through experimentation as the input data.

3. Finite Element Simulation Model

3.1. Hyperelastic material constitutive model

The spokes and shear band of NPT examined in this study were all composed of rubber. A hyperelastic constitutive model was employed in the FEM to simulate these components. The stress–strain relationship of a hyperelastic constitutive model is typically expressed through the strain energy density function, denoted as U. The strain energy density function can take various forms, the most commonly used being a polynomial form based on the theory of continuum mechanics [24]. In continuum mechanics, the deformation gradient is expressed as follows:

$$F = \frac{\partial x}{\partial X} = \frac{\partial x_i}{\partial X_I} e_i e_I, \tag{1}$$

where x represents spatial coordinates, X represents material coordinates, and e_i represents basis vectors.

$$F = J^{\frac{1}{3}} I \bar{F} = J^{\frac{1}{3}} I \left(J^{-\frac{1}{3}} Dx \right). \tag{2}$$

The deformation gradient can be decomposed at this point. The two components jointly constitute the decomposed deformation gradient, namely, the isochoric and volumetric parts.

Similarly, the strain energy of the isotropic hyperelastic material can be decom-posed into the following two parts:

$$U = f\left(\bar{I}_1 - 3,_{1} \bar{I}_2 - 3\right) + g\left(J - 1\right). \tag{3}$$

Let $g = \sum_{i=1}^{N} \frac{1}{D_i} (J-1)^{2i}$,and performing a Taylor expansion,

$$U = \sum_{i+j=0}^{N} C_{ij} \left(\bar{I}_1 - 3\right)^i \left(\bar{I}_2 - 3\right)^i + \sum_{i=1}^{N} \frac{1}{D_i} (J-1)^{2i}, \tag{4}$$

here, J represents the elastic volume ratio, I describes the material distortion, C and D are the material characteristic parameters, and N is the order of the chosen constitutive model. C and D describe the shear characteristics and compressibility of the material, respectively. If expressing incompressibility is desired, the D value can be set to zero. For this constitutive model expression, regardless of the chosen model order N, the initial shear modulus and initial volume modulus values depend solely on the first-order coefficients of the polynomial:

$$\mu_0 = 2\left(C_{10} + C_{01}\right), k_0 = 2 / D_1 . \tag{5}$$

Assuming all $C_{ij} \neq 0 (j \neq 0)$, a simplified polynomial model can be obtained:

$$U = \sum_{i=1}^{N} C_{i0} \left(\bar{I}_1 - 3\right)^i + \sum_{i=1}^{N} \frac{1}{D_i} (J-1)^{2i}. \tag{6}$$

For the simplified polynomial, if N=1, the neo-Hookean (N-H) model is obtained [25]

$$U = C_{10} \left(\bar{I}_1 - 3\right) + \frac{1}{D_1} (J-1)^2 . \tag{7}$$

The neo-Hookean model can accurately simulate small deformations of elastic materials, and various parts of the NPT are subjected to small deformations during loading [26]. Moreover, the neo-Hookean model has only one parameter, C_{10}, and to ensure calculation accuracy, it is convenient for subsequent experimental design and simulation model calculations using the response surface method. Therefore, this study adopted the neo-Hookean hyperelastic constitutive model. To further validate the influence of the strain range of the experimental curve on the neo-Hookean model, four strain ranges (25%, 50%, 75%, and 100%) were selected for evaluation. The fitted curves were compared with the experimental results, as shown in Fig. 2, and the corresponding C_{10} values were 1.003, 0.841, 0.781, and 0.788, respectively. When the strain was 25%, the consistency between the constitutive calculation stress–strain curve and the experimental curve was better, particularly below a strain of 20%, making it more suitable for simulating NPTs.

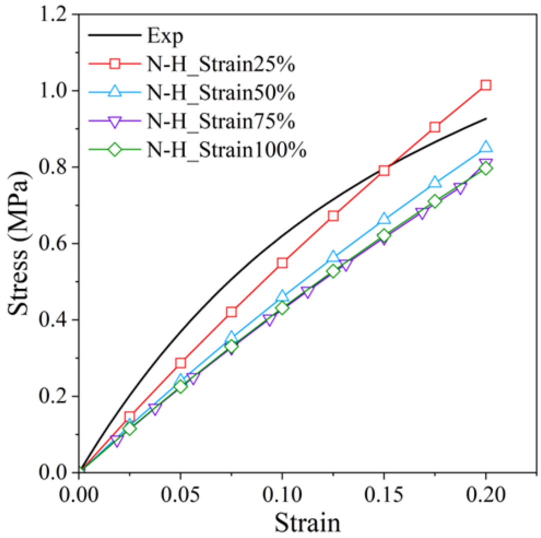

Fig. 2 Comparison of neo-Hookean constitutive fitted curves and experimental results at strains of 25%, 50%, 75%, and 100%

3.2. UPTIS NPT simulation model

3.2.1. Geometric parameters

The NPT model comprised five components: a rim, spoke, reinforcement plate, shear band, and inner/outer belts. The reinforcement plate is shaped like a “V” and is embedded inside the spokes. The ends of the spokes are connected to the inner circle of the shear band and the outer circle of the rim, respectively. The inner and outer belts were embedded in the shear band, forming a shear band. The geometric model in this study was established based on the spoke form by Michelin UPTIS [27].

The UPTIS NPT is intended to replace the 215/50R17 inflatable tire, with a maximum static load capacity of 690 kg. Fig. 3 shows an overview of the established geometric model and spoke structure. Table 1 lists the key geometric parameters and their corresponding values.

3.2.2. Model and operating condition establishment

A three-dimensional simulation model for the NPT was established using the commercial FE analysis software Abaqus, and its vertical loading model is shown in Fig. 4.

The elastic materials for the spokes and shear band in the model were defined as neo-Hookean constitutive

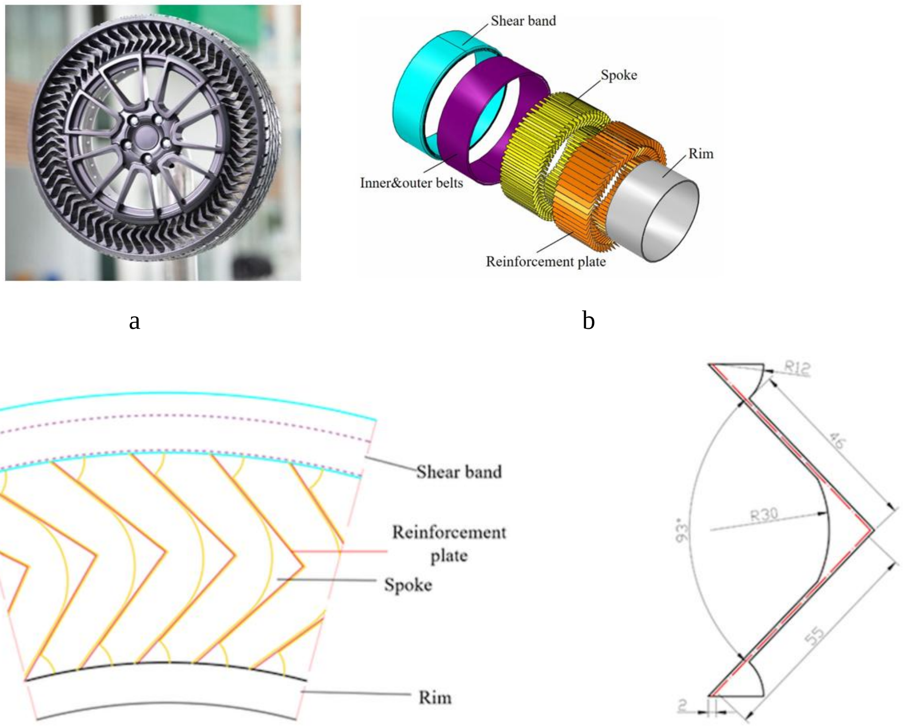

a b

c d

Fig. 3 UPTIS NPT: a – physical view, b – exploded view, c – cross-sectional view, d – spoke size

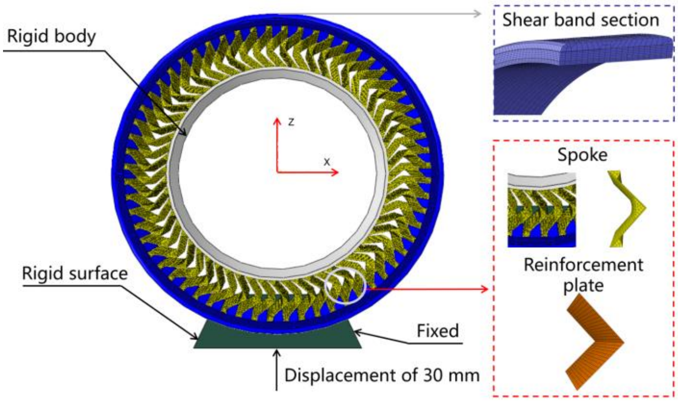

Fig. 4 Finite element simulation model for the vertical loading experiment on an NPT

Table 1

Key design parameters of the UPTIS NPT

Parameter	Outer Diameter, mm	Shear Band Width, mm	Rim Outer Diameter, mm	Rim Width, mm	Shear Band Thickness, mm	Inner Belt Diameter, mm	Outer Belt Diameter, mm
Value	646.8	215	431.8	165.1	14	601.5	626.5

Table 2

Meshing parameters for each component of the npt finite element model

Components	Mesh type	Material parameters	Number of elements
Reinforcement plate	S4R	E=55 GPa	22800
Shear Band	C3D8H	C_{10}=4.0	13728
Inner Belt	SFM3D4R	E=80 GPa	1450
Outer Belt	SFM3D4R	E=80 GPa	1510
Spoke	C3D8H/C3D6H	C_{10}=1.0	66000

models with slightly different C_{10} parameters for each component. The C_{10} values were inversely determined based on the experimental data, for the spokes and shear band, respectively. A hybrid hexahedral/tetrahedral solid element (C3D8H/C3D6H) was selected, and the steel wire reinforcement belt in the shear band was modeled using a linear elastic model with a modulus of 80 GPa and a Poisson's ratio of 0.3; this was defined as a rebar layer element with the element type SFM4D4R. A carbon-fiber composite material plate was adopted for the reinforcing skeleton inside the spoke. The selected composite material had fibers uniformly distributed at an angle, approaching isotropy in mechanical properties. The ultimate strength of the material was 700 MPa [28]. A linear elastic constitutive model with an elastic modulus of 55 GPa and a Poisson's ratio of 0.3 was chosen. It was modeled as a shell element (S4R), and its thickness was 0.5 mm. The meshing details for each part of the NPT are listed in Table 2.

To simulate the road surface, a rigid analysis plane was established, and the NPT FEM was connected with the rigid analysis plane to set up the FEM for vertical stiff-ness testing. A friction coefficient of 0.3 was assumed, and a penalty function was used to calculate the friction force between the shear band and the rigid plane. The contact type between the shear band and the outer ring of the spoke was defined as "Tie", The contact type between each steel layer and the shear band and between the reinforcement plate and the spoke was defined as the "Embedded region". The rim was considered a "Rigid body". In the analysis, the ground was fixed and a downward displacement of 30 mm was applied at the hub center. The resulting reaction force between the NPT and ground was recorded. To calculate the lateral and longitudinal stiffnesses of the NPT, two analysis steps were defined. In the first step, a specific vertical load was applied to the hub center. In the second step, ground displacement of 200 mm was applied along the lateral and longitudinal directions, and the resulting reaction forces and relative displacements between the NPT and the ground were recorded. Because the NPT spokes were arranged asymmetrically, both the forward and reverse directions were considered in the simulation of longitudinal stiffness. The simulation results for each operating condition are presented in Fig. 5.

4. Results and Discussion

4.1. Simulation of vertical stiffness and load-bearing performance

4.1.1. Simulation results

The load–deflection curve obtained from the NPT simulation model under vertical loading is shown in Fig. 6. At a maximum deflection of 30 mm, the corresponding force was 7021 N, meeting the rated load requirements. Linear fitting of the data points yielded the functional expression depicted in the Fig. 6. The vertical force and deflection of the NPT exhibited a clear linear relationship, and the vertical stiffness was approximated as a constant of approximately 234 N/mm.

4.1.2. Analysis of load-bearing principles

During the NPT bearing process, the entire spoke was divided into three zones based on the deformation pattern of a single spoke. The first was the bending-compression hybrid deformation zone, which occurred near the ground contact position. The reinforcement plate in the spoke was bent and the rubber block was compressed. The second zone was the free zone, where there was no significant de-formation of the reinforcement plate or rubber block within the spoke. The third was the bending-tension hybrid deformation zone, which occurred in the upper part of the NPT. In this area, the reinforcement plate in the spoke bent, and the deformation direction was opposite to that of the bottom, causing the rubber block to undergo tension. The spokes undergoing bending-tension hybrid deformation were primarily located in the upper part of the NPT. The tension force exerted on the rim by these spokes was transmitted from the shear bands to the ground. Therefore, the shear bands must possess a certain stiffness to ensure that the top spokes of the NPT have a load-bearing capacity. The load was concentrated in the reinforcement plate section of the overall structure of the NPT. The maximum stress in this section was 490.5 MPa, which was below the ultimate strength of the material. The safety factor was 1.4, which was significantly higher than those of the other rubber material sections. The stress and de-formation nephogram of the rubber section of the NPT structure as shown in Fig. 7.

4.2. Lateral and longitudinal stiffness simulation analysis

4.2.1. Lateral stiffness

The lateral stiffness of the NPT is a crucial indicator related to the steering characteristics of the vehicle and

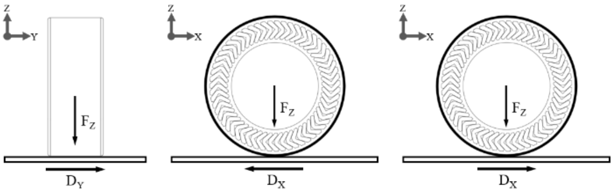

a b c

Fig. 5 Schematic diagram of the stiffness measurement method: a – lateral stiffness, b – longitudinal stiffness (forward), c – longitudinal stiffness (backward)

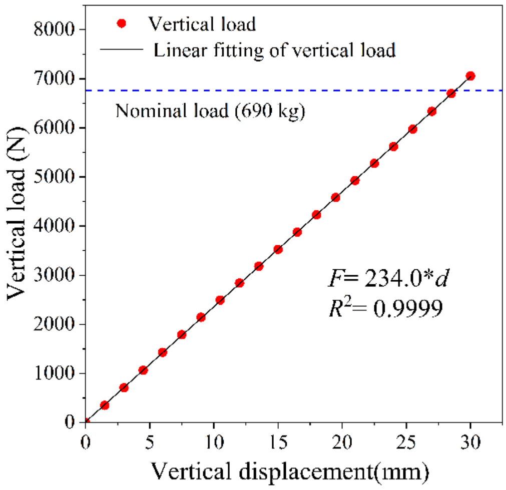

Fig. 6 Relationship curve between vertical load capacity and deflection

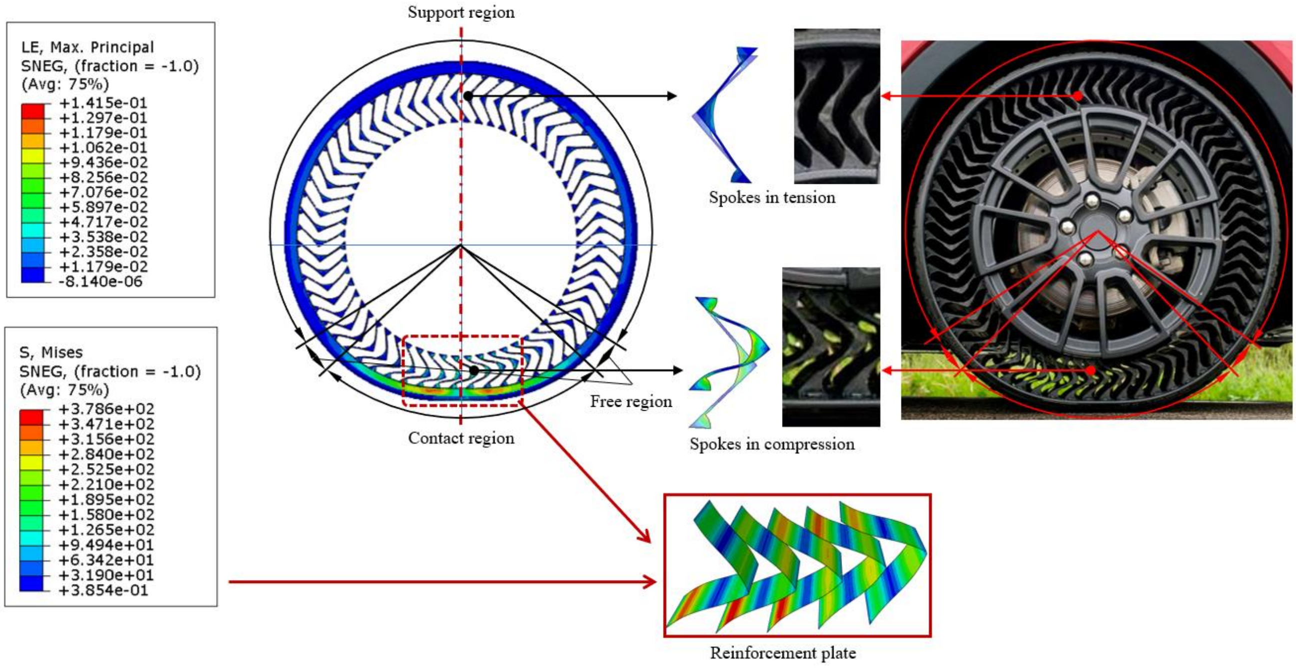

Fig. 7 The deformation mode of NPT under vertical load; stress (S) and strain (LE) nephograms of the main structure

is a primary parameter considered in structural design. The varying deformation of the spokes under different vertical loads has a certain im-pact on the lateral stiffness. Therefore, this study evaluated the lateral loading model of the NPT under vertical loads of 4000 N, 5000 N, 6000 N, and 7000 N and plotted the comparison curve of the lateral force against the lateral displacement (Lateral-D) as shown in Fig. 8. The maximum lateral force after a slip in the curve and the ratio of the relative displacement to the center of the tire footprint were extracted as the lateral stiffness; the calculated values are presented in Table 3. A comprehensive analysis revealed that with an increase in the vertical load, the lateral stiffness increased slightly, but the maximum growth rate was only 14.5%, which was considerably smaller than the rate of change in the vertical load (75%). Therefore, in this study, the change in lateral stiffness was considered to be minimally influenced by the vertical load and could be neglected.

4.2.2. Longitudinal stiffness

The magnitude of the longitudinal stiffness of the NPT affects the driving and braking characteristics of the vehicle. Considering that the circumferential spoke structure of the UPTIS NPT is not axially symmetrical, it is necessary to discuss the longitudinal stiffness in the forward and backward directions separately. In this study, the ground displacement relative to the NPT in the direction of longitudinal displacement, which is consistent with the direction of the tip of the spokes at the bottom of the NPT, was defined as forward, and the opposite direction was considered as backward. The different deformation levels of spokes under different vertical loads have a certain impact on the longitudinal stiffness. Therefore, this study calculated the forward and backward loading models of the NPT under vertical

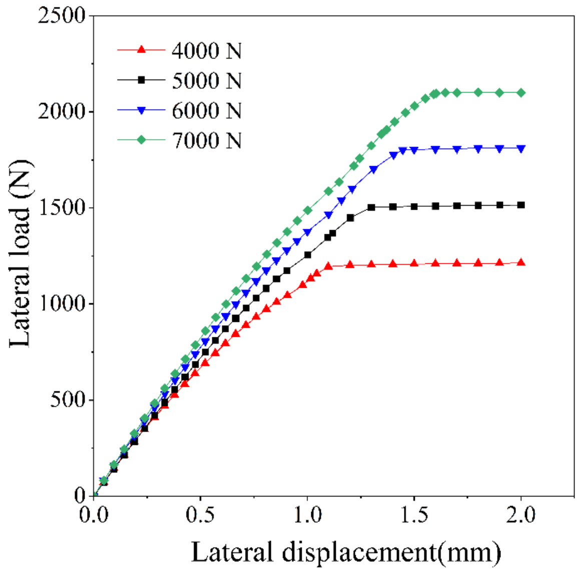

Fig. 8 Relationship between lateral force and displacement under different vertical loads

Table 3

Lateral stiffness calculation results under different vertical loads

No.	Vertical force, N	Theoretical lateral force, N	Lateral force, N	Lateral-*D*, mm	Lateral stiffness, N/mm
1	4000	1200	1211.97	1.14	1067.22
2	5000	1500	1527.62	1.38	1111.14
3	6000	1800	1834.04	1.57	1171.23
4	7000	2100	2139.78	1.75	1221.65

Table 4

Longitudinal stiffness calculation results under different vertical loads

No.	Vertical force, N	Theoretical *L-F*, N	*L-F* (Forward), N	*L-D* (Forward), mm	*L-S* (Forward), N/mm	*L-F* (Backward), N	*L-D* (Backward), mm	*L-S* (Backward), N/mm
1	4000	1200	1196.98	12.19	98.18	1198.69	11.14	107.60
2	5000	1500	1506.64	14.60	103.21	1504.46	13.20	114.00
3	6000	1800	1795.30	16.61	108.08	1796.35	14.94	120.24
4	7000	2100	2103.61	18.42	114.22	2108.02	16.54	127.47

loads of 4000 N, 5000 N, 6000 N, and 7000 N and plotted the comparison curve of the longitudinal force (*L-F*) against the longitudinal displacement (*L-D*) as shown in Fig. 9. The maximum force after a slip in the curve and the ratio of the relative displacement to the center of the tire footprint were extracted as the longitudinal stiffness (*L-S*); the calculated values are given in Table 4. A comprehensive analysis revealed that with an increase in vertical load, the forward and backward longitudinal stiffnesses both slightly increased, but the maximum growth rates were only 16.3% and 18.5%, respectively, which were considerably smaller than the rate of change in the vertical load (75%). Therefore, in this study, it was considered that the change in longitudinal stiffness in the forward and backward directions was minimally influenced by the vertical load and could be neglected.

4.3. Response surface analysis

4.3.1. Experimental design

To analyze the impact of different design parameters on the tri-directional stiff-ness of the NPT, this study considered the internal reinforcement plate thickness (*RP-T*) of the spokes and the material constitutive parameter C_{10} for both the spokes and shear bands as influencing factors, that is, independent variables. The vertical, lateral, and longitudinal stiffness values of the tire were selected as dependent variables for the experimental design and response surface analysis, and the range of reinforcement plate thickness was defined as 0.4-0.6 mm. This was mainly because the total thickness of the bent part of the spoke was 2 mm. While ensuring the vulcanization of the external rubber, when the reinforcement plate thickness exceeded 0.6 mm, the maximum stress on the reinforcement plate under the rated load exceeded the material strength limit (550 MPa). Therefore, 0.6 mm was set as the maximum design value. Simultaneously, through simulation calculations, when the reinforcement plate thickness was less than 0.4 mm, the NPT underwent excessive deformation under the rated load and failed to meet the load-bearing requirements. Hence, 0.4 mm was set as the minimum design value. Shear-band rubber material is typically hard rubber to ensure sufficient support force during shear deformation. The neo-Hookean constitutive parameter C_{10} has a range of 3.0–5.0, corresponding to a rubber hardness of 55–79 Shore A. The spoke rubber material in NPTs primarily connects to and encapsulate the composite-material reinforcement plate, and ordinary wear-resistant rubber is used. The neo-Hookean constitutive parameter C_{10} has a range of 0.5–1.5, corresponding to a rubber hardness of 88–92 Shore A [29]. For these three independent variables, Latin hypercube sampling [30] was conducted within their respective ranges, resulting in 27 experimental models. The de-sign of experiments matrix was constructed as presented in Table 5.

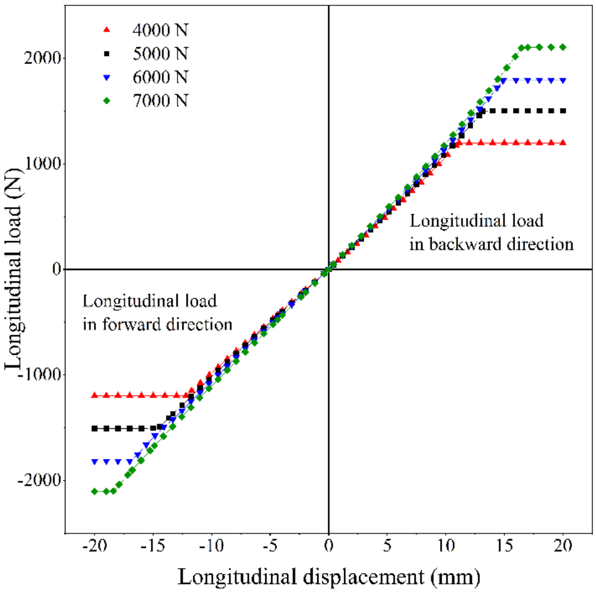

Fig. 9 Relationship between longitudinal force and displacement under different vertical loads

Based on the analysis results shown in Section 4.2, this study selected the vertical stiffness measured at a vertical displacement of 25 mm and the lateral and longitudinal stiffnesses at a vertical load of 4000 N for further analysis and calculation.

4.3.2. Establishment of the response surface for NPT tri-directional stiffness

1. Vertical stiffness

Table 6 lists the vertical stiffness values calculated for the 27 simulation models, and a response surface model for vertical stiffness was fitted using Isight software. Fig. 10 illustrates the relationship between vertical stiffness and the variation in any two independent variables. Vertical stiffness increased with an increase in all three independent variables. The polynomial mathematical model of the response surface is given by Eq. (8), and its coefficients are provided in Table 7. The fitting accuracy was R^2=0.9994.

2. Lateral stiffness

Table 8 lists the lateral stiffness values calculated for the 27 simulation models, and a response surface model for lateral stiffness was fitted using Isight software. Fig. 11 illustrates the relationship between lateral stiffness and the variation in any two independent variables. Lateral stiffness increased with an increase in all three independent variables. The polynomial mathematical model of the response surface is given by Eq. (8), and its coefficients are provided in Table 9.

The fitting accuracy was $R^2=0.9906$.

3. Longitudinal stiffness

Tables 10 and 11 list the longitudinal stiffness values calculated for the 27 simulation models. The Isight software was used to fit the response surface models for longitudinal stiffness in the forward and backward directions. Figs. 12 and 13 depict the relationship between the longitudinal stiffness in the forward and backward directions and the variation in any two independent variables, respectively. The longitudinal stiffness increased with an increase in all three independent variables. The polynomial mathematical model of the response surface for the longitudinal stiffness is given by Eq. (8), and its coefficients are listed in Table 12. The fitting accuracies in the forward and backward directions were $R^2=0.9983$ and 0.9979, respectively.

$$f_{RR}(x,y,z)=C_0+C_1x+C_2y+C_3z+C_4x^2+C_5y^2+C_6z^2+C_7xy+$$
$$+C_8xz+C_9yz+C_{10}x^3+C_{11}y^3+C_{12}z^3+C_{13}x^4+C_{14}y^4+C_{15}z^4. \tag{8}$$

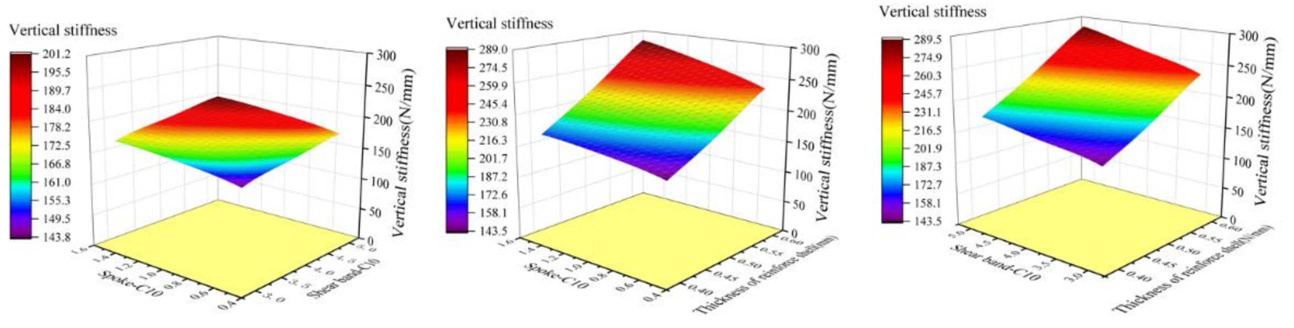

a b c

Fig. 10 Response surface contour maps for vertical stiffness: a – response surface plot of vertical stiffness with respect to spoke C_{10} and shear band C_{10}, b – response surface plot of vertical stiffness with respect to spoke C_{10} and reinforcement plate thickness, c – response surface plot of vertical stiffness with respect to reinforcement plate thickness and shear band C_{10}

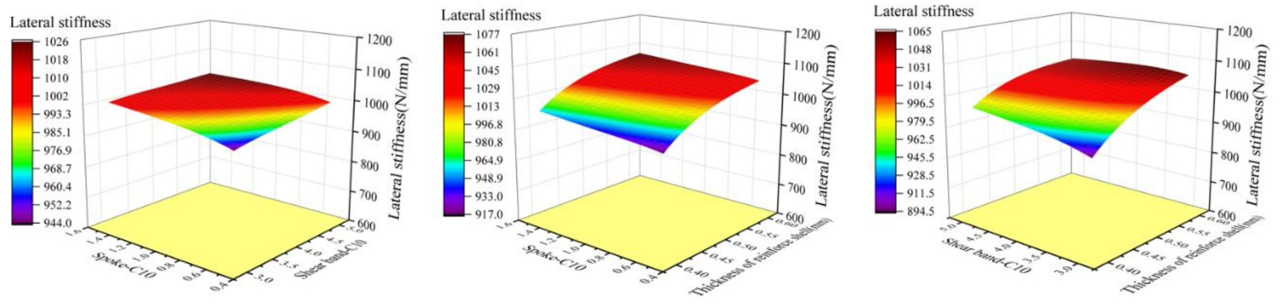

a b c

Fig. 11 Response surface contour maps for lateral stiffness: a – response surface plot of lateral stiffness with respect to spoke C_{10} and shear band C_{10}, b – response surface plot of lateral stiffness with respect to spoke C_{10} and reinforcement plate thickness, c – response surface plot of lateral stiffness with respect to reinforcement plate thickness and shear band C_{10}

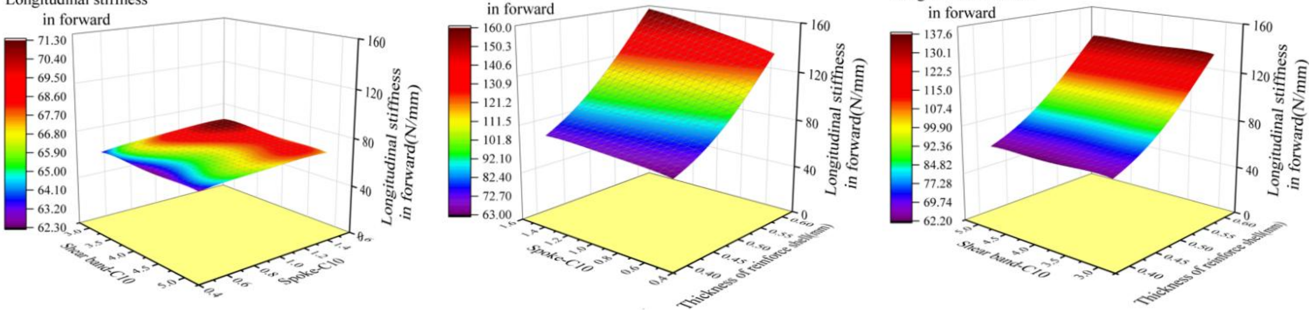

a b c

Fig. 12 Response surface contour maps for longitudinal stiffness (forward): a - response surface plot of longitudinal stiffness (forward) with respect to spoke C_{10} and shear band C_{10}, b - response surface plot of longitudinal stiffness (forward) with respect to spoke C_{10} and reinforcement plate thickness, c - response surface plot of longitudinal stiffness (forward) with respect to reinforcement plate thickness and shear band C_{10}

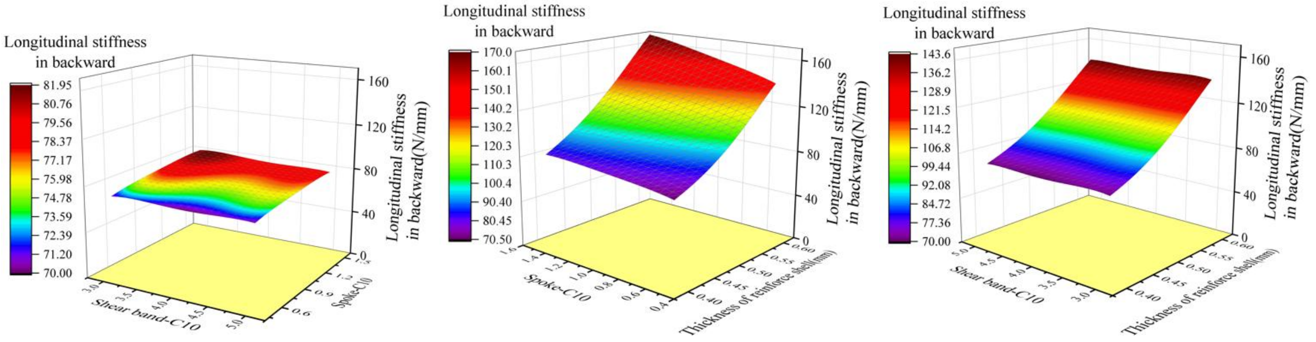

a b c

Fig. 13 Response surface contour maps for longitudinal stiffness (backward): a – response surface plot of longitudinal stiffness (backward) with respect to spoke C_{10} and shear band C_{10}, b – response surface plot of longitudinal stiffness (backward) with respect to spoke C_{10} and reinforcement plate thickness, c – response surface plot of longitudinal stiffness (backward) with respect to reinforcement plate thickness and shear band C_{10}

Table 5

Experimental matrix of the finite element model

No.	Spoke C_{10}	Shear band C_{10}	*RP-T*, mm	No.	Spoke C_{10}	Shear band C_{10}	*RP-T*, mm	No.	Spoke C_{10}	Shear band C_{10}	*RP-T*, mm
1	0.50	3.15	0.46	10	0.85	4.69	0.52	19	1.19	5.00	0.42
2	0.54	4.23	0.45	11	0.88	4.31	0.43	20	1.23	3.85	0.45
3	0.58	4.08	0.59	12	0.92	4.54	0.55	21	1.27	4.00	0.58
4	0.62	3.38	0.48	13	0.96	3.08	0.55	22	1.31	3.00	0.49
5	0.65	4.15	0.54	14	1.00	3.92	0.41	23	1.35	4.85	0.44
6	0.69	3.46	0.58	15	1.04	3.54	0.48	24	1.38	4.38	0.42
7	0.73	3.31	0.53	16	1.08	4.62	0.52	25	1.42	4.46	0.50
8	0.77	3.23	0.57	17	1.12	3.69	0.56	26	1.46	4.77	0.40
9	0.81	4.92	0.60	18	1.15	3.62	0.47	27	1.50	3.77	0.51

Table 6

Simulation results for vertical stiffness

No.	Vertical force, N	Vertical stiffness, N/mm	No.	Vertical force, N	Vertical stiffness, N/mm	No.	Vertical force, N	Vertical stiffness, N/mm
1	4350.64	174.03	10	6402.22	256.09	19	5260.11	210.40
2	4698.02	187.92	11	4881.32	195.25	20	5247.17	209.89
3	6687.77	267.51	12	6792.83	271.71	21	7351.17	294.05
4	4908.10	196.32	13	6074.90	243.00	22	5384.28	215.37
5	6102.87	244.11	14	4476.81	179.07	23	5540.70	221.63
6	6433.06	257.32	15	5294.04	211.76	24	5008.94	200.36
7	5638.67	225.55	16	6482.36	259.29	25	6415.80	256.63
8	6179.04	247.16	17	6757.72	270.31	26	4965.10	198.60
9	7715.42	308.62	18	5303.58	212.14	27	6217.44	248.70

Table 7

Coefficients for the vertical stiffness fitting equation

C_0	C_1	C_2	C_3	C_4	C_5	C_6	C_7
-4006.65	127.88	1596.55	20718.44	-226.88	-603.48	-65241.09	1.36
C_8	C_9	C_{10}	C_{11}	C_{12}	C_{13}	C_{14}	C_{15}
142.65	54.98	139.89	99.95	91066.20	-33.23	-6.15	-47041.14

Table 8

Simulation results for lateral stiffness

No.	Lateral force, N	Lateral-*D*, mm	Lateral stiffness, N/mm	No.	Lateral force, N	Lateral- *D*, mm	Lateral stiffness, N/mm	No.	Lateral force, N	Lateral-*D*, mm	Lateral stiffness, N/mm
1	1221.51	1.28	953.10	10	1219.76	1.18	1036.95	19	1221.11	1.23	990.66
2	1221.15	1.25	980.82	11	1221.06	1.24	980.81	20	1220.33	1.21	1004.50
3	1219.04	1.16	1047.82	12	1219.36	1.17	1045.77	21	1218.76	1.14	1064.45
4	1221.13	1.23	991.11	13	1220.17	1.18	1037.10	22	1220.60	1.21	1011.90
5	1219.72	1.18	1037.64	14	1221.04	1.29	945.53	23	1220.79	1.21	1005.99
6	1218.93	1.16	1046.34	15	1220.44	1.21	1008.84	24	1220.97	1.25	980.27
7	1220.28	1.19	1023.84	16	1219.74	1.17	1040.44	25	1219.80	1.17	1043.21
8	1219.72	1.17	1039.86	17	1218.98	1.15	1057.34	26	1221.23	1.26	969.75
9	1219.28	1.16	1050.85	18	1220.32	1.21	1008.92	27	1219.50	1.16	1047.46

Table 9

Coefficients for the lateral stiffness fitting equation

C_0	C_1	C_2	C_3	C_4	C_5	C_6	C_7
-4180.60	373.72	983.95	22755.86	-359.70	-277.22	-51086.73	-15.85
C_8	C_9	C_{10}	C_{11}	C_{12}	C_{13}	C_{14}	C_{15}
-4180.60	373.72	983.95	22755.86	-359.70	-277.22	-51086.73	-15.85

Table 10

Longitudinal stiffness (forward) simulation results

No.	*L-F*, N	*L-D*, mm	*L-S*, N/mm	No.	*L-F*, N	*L-D*, mm	*L-S*, N/mm	No.	*L-F*, N	*L-D*, mm	*L-S*, N/mm
1	1203.93	15.39	78.24	10	1199.75	11.15	107.61	19	1197.52	16.36	73.18
2	1196.72	16.31	73.37	11	1196.82	16.31	73.38	20	1196.46	14.19	84.31
3	1202.61	8.94	134.55	12	1200.53	10.00	120.03	21	1202.86	8.44	142.58
4	1201.28	13.58	88.43	13	1198.10	9.55	125.46	22	1202.50	11.90	101.04
5	1199.62	10.82	110.91	14	1199.79	17.57	68.28	23	1197.04	15.12	79.17
6	1203.48	8.90	135.23	15	1198.79	13.10	91.48	24	1197.35	16.51	72.54
7	1201.02	10.93	109.89	16	1199.56	11.16	107.53	25	1198.81	11.50	104.25
8	1199.32	9.28	129.29	17	1202.54	9.11	131.94	26	1199.46	17.51	68.49
9	1200.76	8.25	145.61	18	1198.02	13.37	89.57	27	1198.23	11.00	108.93

Table 11

Longitudinal stiffness (backward) simulation results

No.	*L-F*, N	*L-D*, mm	*L-S*, N/mm	No.	*L-F*, N	*L-D*, mm	*L-S*, N/mm	No.	*L-F*, N	*L-D*, mm	*L-S*, N/mm
1	1204.88	14.00	86.08	10	1199.88	10.27	116.80	19	1198.23	14.33	83.63
2	1195.34	14.66	81.56	11	1195.30	14.41	82.98	20	1196.58	12.59	95.02
3	1202.67	8.54	140.87	12	1200.73	9.29	129.26	21	1203.31	7.89	152.58
4	1202.38	12.41	96.86	13	1198.33	8.91	134.52	22	1201.46	10.75	111.72
5	1200.10	10.10	118.86	14	1198.18	15.36	78.01	23	1198.05	13.30	90.10
6	1203.56	8.45	142.40	15	1199.42	11.80	101.68	24	1195.28	14.37	83.18
7	1200.87	10.15	118.27	16	1199.85	10.20	117.63	25	1199.46	10.40	115.36
8	1199.56	8.74	137.20	17	1203.21	8.50	141.58	26	1196.01	15.14	78.98
9	1200.71	7.82	153.51	18	1198.39	11.97	100.11	27	1200.13	9.98	120.25

4.3.3. Parameter analysis results

Within the range of the independent variables, the stiffness in all directions of the NPT increased with an increase in the spoke rubber material C_{10}, shear band rubber material C_{10}, and reinforcement plate thickness. Among the set range of independent variables, the maximum value of the vertical stiffness was 308.61 N/mm, and the minimum was 143.95 N/mm. The maximum lateral stiffness value was 1064.44 N/mm, and the minimum was 876.23 N/mm. The maximum longitudinal stiffness (forward) was 145.61 N/mm, and the minimum was 62.31 N/mm. The maximum value of the longitudinal stiffness (backward) was 153.51 N/mm, and the minimum was 70.04 N/mm. The lateral stiffness of the NPT was significantly greater than the stiffness in other directions.

By employing response surface models tailored for vertical, lateral, and longitudinal stiffnesses, we can compute partial derivatives with respect to their respective independent variables. The magnitude of the partial derivative at a specific point within the domain indicated the extent to which the independent variable influenced the dependent variable at that point. A higher absolute value indicated a greater impact.

Utilizing the response surface models tailored for vertical, lateral, and longitudinal stiffnesses allowed the calculation of partial derivatives with respect to their respective independent variables. The absolute value of the partial derivative at a specific point within the domain indicated the degree to which the independent variable influenced the dependent variable at that point; a larger absolute value indicated a more significant influence. The average of the absolute values of the partial derivatives within the domain provided the average gradients for the independent variable within its designated range.

Given the disparate ranges of the independent variables, the direct use of the average gradients within the domain may not provide a meaningful comparison of their impacts. Considering the nearly monotonic changes observed in the response surface models for the vertical, lateral, and longitudinal stiffnesses with variations in their respective independent variables, an approximate assessment of the influence can be made by multiplying the average rate of change by the size of the variable's range. The specific values are listed in Table 13.

By comparing the average rate of change of the independent variables and the composite impact values, the variation in the reinforcement plate thickness was found to have a more significant impact on the three-dimensional stiffness of the NPT than the other two variables. The thickness of the reinforcement plate was the most critical influencing parameter. Furthermore, the spoke material constitutive parameter C_{10} and shear band material constitutive parameter C_{10} had a fairly equal influence on both the vertical and lateral stiffnesses. The longitudinal stiffness was slightly more affected by the spoke material constitutive parameter C_{10} than by the shear band material constitutive parameter C_{10}. This conclusion aligns with the observation that the stress is primarily concentrated on the reinforcement plate in the FEM, highlighting the reinforcement plate as the main load-bearing component in the structure.

Table 12

Coefficients for the longitudinal stiffness fitting equation

	C_0	C_1	C_2	C_3	C_4	C_5	C_6	C_7
Forward	-1682.93	80.77	1019.98	6623.47	-158.59	-387.22	-22850.75	-1.38
Backward	-2022.68	90.02	1100.38	8703.13	-168.82	-416.82	-29000.24	-1.50
	C_8	C_9	C_{10}	C_{11}	C_{12}	C_{13}	C_{14}	C_{15}
Forward	84.57	5.03	107.84	64.43	34333.09	-27.29	-3.97	-18385.20
Backward	94.68	6.95	112.13	69.16	42374.57	-28.00	-4.25	-22357.32

Table 13

Sensitivity analysis

		RP-T, mm	Spoke C_{10}	Shear band C_{10}
Domain		0.2	1	2
Vertical Stiffness	Average Gradients	578.63	40.04	22.00
	Impact Value, N/mm	115.72	40.04	44.00
Lateral Stiffness	Average Gradients	650.56	36.03	21.62
	Impact Value, N/mm	130.11	36.03	43.25
Longitudinal Stiffness (Forward)	Average Gradients	401.07	14.33	3.15
	Impact Value, N/mm	80.21	14.33	6.31
Longitudinal Stiffness (Backward)	Average Gradients	395.52	18.26	3.40
	Impact Value, N/mm	79.10	18.26	6.80

Table 14

Comparison of optimization results

Property	Spoke C_{10}	Shear band C_{10}	*RP-T*, mm	Vertical stiffness, N/mm	Lateral stiffness, N/mm	*L-S* (Forward), N/mm	*L-S* (Backward), N/mm
Standard	1.0	4.0	0.5	234	1067.22	98.18	107.06
Optimized from RSM	0.54	3.0	0.6	239.51	1033.5	137.08	142.51
Optimized from FEM	0.54	3.0	0.6	239.80	1043.47	134.22	138.40
Relative Error				0.12%	0.95%	2.13%	2.96%

4.3.4. Multiple objectives of optimization based on the response surface model

The vertical stiffness of an NPT is directly correlated with its load-carrying capacity, and its significance is prioritized in the design process to ensure an ample load-carrying capacity. When designing the lateral and longitudinal stiffnesses, the objective is typically to achieve greater values for effective steering response and braking performance. According to the response surface model and sensitivity analysis mentioned above, the maximum rate of change in the lateral stiffness within the range of independent variables was only 21.5%. This was mainly influenced by the thickness of the composite material reinforcement plate. Given the substantially larger value of the lateral stiffness compared to the vertical and longitudinal stiffnesses, it was not considered an optimization target in this multi-objective optimization. The primary focus was on attaining a higher longitudinal stiffness while maintaining the vertical stiffness.

Using the Isight software, multi-objective optimization was performed on the response surface model to ensure the load-bearing capacity. The vertical stiffness was constrained within the range 230–240 N/mm. The optimization was primarily aimed at maximizing the longitudinal stiffness in both the forward and backward directions. The stiffness values for each direction under the optimized and standard variable parameters are presented in Table 14.

By comparing the optimized results with the standard values, the optimized vertical stiffness was found to increase by 2.3% and remained relatively stable. The lateral stiffness decreased by 3.1% while remaining at the same level. The longitudinal stiff-ness in the forward direction increased by 39.1% and the backward longitudinal stiff-ness increased by 32.9%. After optimization, while maintaining the vertical and lateral stiffnesses, there was a significant improvement in the longitudinal stiffness. This optimization achieved a substantial enhancement in the braking responsiveness while ensuring the load capacity and high steering performance of the NPT.

5. Conclusions

To predict the triaxial stiffness of NPTs, FE simulation calculations were con-ducted on the UPTIS NPT structure under vertical, lateral, and longitudinal loadings using three design variables: 1. the shear band material constitutive parameter C_{10}, 2. spoke material constitutive parameter C_{10}, and 3. reinforcement plate thickness. The simulation results provided different stiffness values for the NPT in the vertical, lateral, and longitudinal directions for various parameter combinations. Mathematical fitting was applied to the experimental data, and a response surface model for the triaxial stiffness of the UPTIS NPT structure was constructed. The main findings of this study are as follows.

1. A simulation model was established for the NPT with a UPTIS composite spoke structure, and the vertical load-carrying principles were analyzed. The load is concentrated on the reinforcement plate, where the maximum stress reaches 490.5 MPa;

2. The response surface method was used to analyze the impact of the structural and material parameters on the vertical, lateral, and longitudinal stiffnesses of the NPT. The results indicated that reinforcement plate thickness was the most significant influencing factor, with the comprehensive influence values for the vertical, lateral, forward, and rearward directions reaching 115.72, 13.11, 50.21, and 79.10, respectively;

3. A mathematical model was established for predicting the three-dimensional stiffness of the UPTIS NPT structure under different material properties, and a model was provided for selecting the independent variable parameters based on the required stiffness;

4. A multi-objective optimization of the design parameters of the UPTIS NPT structure was based on the response surface model. While ensuring the load capacity and steering performance, the longitudinal stiffness in the forward and backward directions was increased by 39.1% and 32.9%, respectively. The optimization process resulted in increased longitudinal stiffness and improved the braking response performance of the NPT.

NPTs offer significant flexibility in terms of their structural and material design. This study proposed a design approach to predict the variation in the three-dimensional stiffness of an NPT with different design parameters. In future work, further exploration can be conducted to investigate the mathematical relationships between additional parameters and the dynamic characteristics of NPTs.

References

1. **Rhyne, T. B.; Cron, S. M.** 2006. Development of a non-pneumatic wheel, Tire Science and Technology 34(3): 150–169. https://doi.org/10.2346/1.2345642.
2. **Bezgam, S.** 2009. Design and Analysis of Alternating Spoke Pair Concepts for a Non-pneumatic Tire with Reduced Vibration at High Speed Rolling. Master’s Thesis, Clemson University, Clemson, SC, USA.
3. **Ju, J.; Kim, D. M.; Kim, K**. 2012. Flexible cellular solid spokes of a non-pneumatic tire, Composite Structures 94(8): 2285-2295. https://doi.org/10.1016/j.compstruct.2011.12.022.
4. **Zhao, Y.Q.; Zang, L.G.; Chen, Y.Q.** 2015. Non-pneumatic mechanical elastic wheel natural dynamic characteristics and influencing factors. Journal of Central South University. 22, 1707-1715. https://doi.org/10.1007/s11771-015-2689-1.
5. **Kim, K.; Kim, D**. 2010. Contact Pressure of Non-Pneumatic Tires with Auxetic Honeycomb Spoke, Journal of Aerospace System Engineering 4: 1-9. https://doi.org/10.5139/JKSAS.2011.39.8.719.
6. MICHELIN Uptis. Available online: https://michelinmedia.com/michelin-uptis/
7. **Gasmi, A.; Joseph, P. F.; Rhyne, T. B.; Cron, S. M.** 2011. Closed-form solution of a shear deformable, extensional ring in contact between two rigid surfaces, International Journal of Solids and Structures 48(5): 843-853. https://doi.org/10.1016/j.ijsolstr.2010.11.018.
8. **Gasmi, A.; Joseph, P. F.; Rhyne, T. B.; Cron, S. M.** 2012. Development of a two-dimensional model of a compliant non-pneumatic tire, International Journal of Solids and Structures 49(13), 1723-1740. https://doi.org/10.1016/j.ijsolstr.2012.03.007.
9. **Rugsaj, R.; Suvanjumrat, C.** 2018. Finite element

analysis of hyperelastic material model for nonpneumatic tire, Key Engineering Materials 775: 554-559. https://doi.org/10.4028/www.scientific.net/KEM.775.554.

10. **Rugsaj, R.; Suvanjumrat, C.** 2022. Study of geometric effects on nonpneumatic tire spoke structures using finite element method, Mechanics Based Design of Structures and Machines 50(7): 2379-2399. https://doi.org/10.1080/15397734.2020.1777875.
11. **Rugsaj, R.; Suvanjumrat, C.** 2019. Proper radial spokes of non-pneumatic tire for vertical load supporting by finite element analysis, International Journal of Automotive Technology 20: 801-812. https://doi.org/10.1007/s12239-019-0075-y.
12. **Żmuda, M.; Jackowski, J.; Hryciów, Z.** 2019. Numerical research of selected features of the non-pneumatic tire, AIP Conference Proceedings 2078(1): 020027. https://doi.org/10.1063/1.5092030.
13. **Hryciów, Z.; Jackowsk,i J.; Żmuda, M.** 2020. The Influence of Non-Pneumatic Tyre Structure on its Operational Properties, International Journal of Automotive and Mechanical Engineering 17(3): 8168-8178. https://doi.org/10.15282/ijame.17.3.2020.10.0614.
14. **Jin, X.; Hou, C.; Fan, X.; Sun, Y.; Lv, J.; Lu, C.** 2018. Investigation on the static and dynamic behaviors of non-pneumatic tires with honeycomb spokes, Composite Structures 187: 27-35. https://doi.org/10.1016/j.compstruct.2017.12.044.
15. **Ganniari-Papageorgiou, E.; Chatzistergos, P.; Wang, X. X.** 2020. The Influence of the Honeycomb Design Parameters on the Mechanical Behavior of Non-Pneumatic Tires, International Journal of Applied Mechanics 12(3): 2050024. https://doi.org/10.1142/S1758825120500246.
16. **Zhao, Y. Q.; Du X. B.; Lin F.; Wang, Q.; Fu, H.** 2018. Static stiffness characteristics of a new non-pneumatic tire with different hinge structure and distribution, Journal of Mechanical Science and Technology 32: 3057-3064. https://doi.org/10.1007/s12206-018-0608-8.
17. **Lee, C.; Ju, J.; Kim, D. M.** 2012. The Dynamic Properties of a Non-Pneumatic Tire With Flexible Auxetic Honeycomb Spokes, ASME International Mechanical Engineering Congress and Exposition 8: 605-615. https://doi.org/10.1115/IMECE2012-88199.
18. **Liu, W. D.; Liu, S.; Li, X. J.; Zhang, Q.; Wang, C.; Li, K.** 2023. Static Stiffness Properties of High Load Capacity Non-Pneumatic Tires with Different Tread Structures, Lubricants 11(4): 180. https://doi.org/10.3390/lubricants11040180.
19. **Liang, X. M.; Fu, H. X.; Wang, Y.; Ku, L.; Qiao, H.; Li, N.** 2022. Study of composite load-bearing characteristics of the Uptis non-pneumatic tyre, International Journal of Vehicle Systems Modelling and Testing 16(1): 79-93. https://doi.org/10.1504/IJVSMT.2022.126973.
20. **Dhrangdhariya, P.; Maiti, S.; Rai, B.** 2021. Effect of spoke design and material nonlinearity on non-pneumatic tire stiffness and durability performance, arXiv preprint arXiv: 2103.03637. https://doi.org/10.48550/arXiv.2103.03637.
21. **Dhrangdhariya, P.; Maiti, S.; Rai, B.** 2024. Topological Optimization of Non-Pneumatic Unique Puncture-Proof Tire System Spoke Design for Tire Performance, SAE International Journal of Passenger Vehicle System 17(1): 3-23. https://doi.org/10.4271/15-17-01-0001.
22. **Kim, K.; Heo, H.; Uddin, M.; Ju, J.; Kim, D. M.** 2015. Optimization of Nonpneumatic Tire with Hexagonal Lattice Spokes for Reducing Rolling Resistance, SAE Technical Paper 1515: 1-10. https://doi.org/10.4271/2015-01-1515.
23. **Liu, X.Y.; Xu, T.; Zhu L. L.; Gao, F.** 2022. Multi-Objective Optimization of the Geometry of a Non-Pneumatic Tire for Three-Dimensional Stiffness Adaptation, Machines 10(12): 1183. https://doi.org/10.3390/machines10121183.
24. **Jaszak, P.** 2016. Modelowanie gumy za pomocą metody elementów skończonych (Modelling of the rubber in Finite Element Method), Elastomery 20(3): 31-39.
25. **Phromjan, J.; Suvanjumrat, C.** 2021. Optimized Stress-Strain Ranges for Hyperelastic Constitutive Models Supporting the Simulation of Vertical Stiffness on Airless Tire, IOP Conference Series: Materials Science and Engineering 1063: 012002. https://doi.org/10.1088/1757-899X/1063/1/012002.
26. **Sun, M.; Liu, W.; Zhang, Q.; Chen, Y.; Jiang, J.; Liu, X.** 2024. Study on the Load-Bearing Characteristics Analysis Model of Non-Pneumatic Tire with Composite Spokes, Machines 12(6): 358. https://doi.org/10.3390/machines12060358.
27. **Miles, K. C.; Cron, S. M.** 2023. Reinforced resilient support for a non-pneumatic tire, U.S. Patent No. 11,577,549.
28. **Zhao, G. P.; Wang, Z.H.; Zhang, J.X.; Huang, Q. P.** 2007. Modeling and Testing Strain Rate-Dependent Tensile Strength of Carbon/Epoxy Composites, Key Engineering Materials 353: 1418-1421. https://doi.org/10.4028/www.scientific.net/KEM.353-358.1418.
29. **Wang, W.; Deng, T.; Zhao, S.G.** 2004. Determination for material constants of rubber Mooney-Rivlin model, Special Purpose Rubber Products 4: 8-10.
30. **Huntington, D. E.; Lyrintzis, C. S.** 1998**.** Improvements to and limitations of Latin hypercube sampling, Probabilistic Engineering Mechanics 13(4): 245-253. https://doi.org/10.1016/S0266-8920(97)00013-1.

J. C. Liang, X. T. Liu, X. J. Wu, M. Y. Sun, Y. X. Song, W. D. Liu, Q. S. Zhang

OPTIMIZATION OF STATIC THREE-DIMENSIONAL STIFFNESS OF NON- PNEUMATIC TIRE WITH COMPOSITE SPOKES BASED ON RESPONSE SURFACE METHOD

Summary

This study aimed to investigate the relationship between the static stiffness of non-pneumatic tires (NPTs) and the design parameters of composites spokes and shear bands using the finite element (FE) method. The stress–strain curve of the rubber material was fitted using the neo-Hookean constitutive model. Subsequently, key design parameters, including the reinforcement plate thickness and constitutive parameters of the spoke and shear band materials, were selected based on the NPT structure. FE simulations were performed on multiple sets of different parameter design schemes for the NPTs, and polynomial models for the vertical, lateral, and longitudinal stiffnesses were established using response surface analysis. The sensitivity analysis results indicated that the thickness of the reinforcement plate significantly influenced the three-dimensional stiffness, whereas the constitutive parameters of the spoke and shear band materials had a relatively minor impact. Finally, multi-objective optimization was employed to determine a design scheme with maximum longitudinal stiffness while ensuring vertical load-bearing capacity. Under the premise of ensuring the vertical load-bearing capacity, the longitudinal stiffness increased by 39.1% and 32.9% in the forward and backward directions, respectively. This method can be used to predict the three-dimensional stiffness of NPTs under different design parameter schemes or to optimize the setting parameters of NPTs based on the desired target stiffness, facilitating the rapid design of the three-dimensional stiffness of NPTs.

Keywords: non-pneumatic tire, finite element analysis, three-dimensional stiffness, composite material spokes, response surface analysis.

Received January 31, 2025
Accepted April 22, 2025